JOURNAL OF GUIDANCE, CONTROL, AND DYNAMICS
Vol. 23, No. 6, November–December 2000

Tensegrity Flight Simulator

Cornel Sultan* and Martin Corless†
Purdue University, West Lafayette, Indiana 47907-1282
and
Robert E. Skelton‡
University of California, San Diego, California 92093-0411

In this paper we propose a new motion simulator based on a tendon-controlled tensegrity structure. The simulator is equipped with a nonlinear controller that achieves robust tracking of desired motions. The controller parameters can be tuned to guarantee tracking to within a prespecified tolerance and with a prescribed rate of exponential convergence. The design is verified through numerical simulations for specific longitudinal motions of a symmetric aircraft.

Nomenclature

b	=	side length of the base and cabin triangles
C_d	=	aerodynamic coefficient of drag
C_l	=	aerodynamic coefficient of lift
C_M	=	aerodynamic coefficient of the pitching moment
$\tilde{c}$	=	mean aerodynamic chord of aircraft wing
D	=	drag
D_r	=	rest-length of diagonal tendons
D_0	=	length of diagonal tendons in a prestressable configuration
g	=	gravitational acceleration constant of the Earth
h_g	=	overlap
I	=	identity matrix
J	=	inertia matrix of the simulator's second stage
J_a	=	aircraft moment of inertia around the pitch axis
K	=	Hessian of the potential energy
k	=	tendon stiffness
k_i^a	=	stiffness of the ith active tendon
k_n	=	stiffness of the nth tendon
L	=	lift
l	=	length of bars
l_i^a	=	length of the ith active tendon
l_n	=	length of the nth tendon
$l_{r_i}^a$	=	rest-length of the ith active tendon
l_{r_n}	=	rest-length of the nth tendon
$M(\boldsymbol{q})$	=	tensegrity simulator inertia matrix
M_t	=	mass of the second stage
M_y	=	aerodynamic pitching moment about the aircraft mass center
m_a	=	aircraft mass
n_u	=	number of active tendons
P	=	pretension coefficient
$\boldsymbol{q}$	=	generalized coordinates vector for simulator
$\boldsymbol{q}_a$	=	generalized coordinates vector for aircraft
$\boldsymbol{q}_g$	=	simulator equilibrium configuration
$\boldsymbol{q}_0$	=	simulator prestressable configuration
$\tilde{\boldsymbol{q}}$	=	tracking error
r	=	tracking tolerance
S	=	lifting surface of the wing
S_r	=	rest-length of saddle tendons
S_0	=	length of saddle tendons in a prestressable configuration
T_D	=	tension in diagonal tendons in a prestressable configuration
T_S	=	tension in saddle tendons in a prestressable configuration
T_n	=	tension in the nth tendon
T_r	=	aircraft thrust
$\boldsymbol{T}^a$	=	vector of tensions in active tendons
$\boldsymbol{T}^p$	=	vector of tensions in passive tendons
t	=	time
V	=	potential elastic energy
v	=	aircraft speed
X, Y, Z	=	Cartesian coordinates of the mass center of the second stage
X_a	=	aircraft horizontal range
Z_a	=	aircraft altitude
α_a	=	aircraft angle of attack
γ	=	rate of exponential convergence
δ_e	=	elevator deflection angle
δ_f	=	flap deflection angle
θ_a	=	aircraft pitch angle
ρ_a	=	air density
τ	=	time constant
ψ, ϕ, θ	=	Euler angles of the second-stage reference frame
ω_y	=	aircraft pitch rate

Introduction

The credit for making simulated flight a reality goes to Edwin Link for providing aviation with the first fixed-based flight trainer. Link's trainer of 1932 was, in the inventor's words, part piano, part pipe organ, and a little bit of airplane,[1] and it played a major part in aviation training for the first 20 years of commercial and military flight. Since then the technology of flight simulation has kept pace with the technological advances in the aerospace industry.

The six-degree-of-freedom (DOF) Stewart platform is the most popular motion base for flight/motion simulators.[2] A very advanced six-DOF Stewart platform flight simulator is the one operated by NASA Ames at Moffett Field, California. This simulator, which became operational in 1993, is an exact replica of the cockpit of a United Airlines Boeing 747-400 and it has unique research capabilities. A detailed description of this facility can be found in Sullivan and Soukup[3] and Blake.[4]

The Stewart platform is a complex and expensive mechanism because the control of its motion presents great technological difficulties because of the telescopic actuators. It is a well-known fact in motion simulators circles that the operation of a telescopic actuator presents difficulties, especially at large amplitudes and large accelerations. This is because of the large and rapid excursions of the actuators, generating large loads on the structure of the simulator. These loads, of both an inertial and dissipative nature, result in a heavy structure and a large associated cooling system. The life of a

Received 10 May 1999; revision received 2 February 2000; accepted for publication 7 February 2000.

*Research Assistant, School of Aeronautics and Astronautics; currently at Molecular Geodesics Inc., Boston, MA 02119. Member AIAA.
†Professor, School of Aeronautics and Astronautics.
‡Professor, Department of Engineering Mechanics. Fellow AIAA.

telescopic actuator is also limited because of the significant wearing that occurs during its operation.

To reduce the complexity of the motion base, there has been renewed interest in reduced-DOF simulators. However, relatively little work has been devoted to the design of reduced-DOF motion bases or to the evaluation of the quality of motion sensations that can be produced by these devices.[5] Pouliot et al.[6] analyzed the simulation realism that can be achieved using motion bases with only three DOF; the advantage of the reduced complexity of the design is important for large transport aircraft for which it produces good quality motion simulation. The weak point of the proposed three-DOF simulators is their inability to simulate high frequency accelerations (see Pouliot et al.[6]). Also, because the motion of the reduced DOF simulators is controlled by telescopic actuators, the problems associated with these actuators are not eliminated.

Another important problem for motion simulators is that of control system design. Many control synthesis techniques have been applied to simulator motion control system design, including classical, adaptive,[7,8] and optimal control.[9,10] Reid and Nahon[11] and Nahon and Reid[12] implemented classical, adaptive, and optimal control algorithms on the University of Toronto Institute for Aerospace Studies six-DOF flight simulator to obtain pilot evaluations of the corresponding motion quality. They indicated that classical and adaptive algorithms are generally preferred by pilots. As a result, a combination of the best features of classical and adaptive schemes into a hybrid scheme was later performed, including the incorporation of nonlinear adaptive filters.[13]

Additional difficulties in the control of motion simulators result from uncertainties in the simulator dynamics. These uncertainties are due, for example, to changes in the simulator inertial properties and uncertainties in the drive system dynamics. Hence, a robust control design strategy should be applied. Idan and Sahar[14] proposed a robust controller for a six-DOF flight simulator. The controller design is based on a linearized model of the simulator dynamics together with an uncertainty model that describes the variation of the simulator weight. The design is performed using μ-synthesis techniques and the controller is designed for lateral motion simulation, for which the linearized model of a DC-8 aircraft is used. Numerical simulations show that good quality lateral motion simulation is achieved.

In this paper we propose a six-DOF motion simulator that eliminates the problems created by telescopic actuators. The structure of the simulator is a tensegrity structure that has no bar to bar connections and no rigid bodies sliding with respect to each other. The motion of the simulator is controlled by tendons, leading to the elimination of telescopic actuators.

A tensegrity structure is a special type of space structure composed of a set of tendons that are prestressed against a system of rigid bodies, usually bars.[15] Tensegrity structures offer excellent opportunities for physically integrated structure and controller design because the elastic components provide excellent opportunities for the sensing and actuating functions.

Although the origins of tensegrity structures can be pinpointed to 1927 (see Snelson[16]), the main investigations have been carried out during the last 40 years. Tensegrity structures were looked on from an engineering perspective for the first time by Fuller.[17] Geometrical investigations followed, most of them being reported in Fuller[17] and Pugh.[18] Approaches using mechanics have been developed recently and research into tensegrity structures has become systematic and aimed at establishing the theoretical framework for the analysis and design of these structures. Pellegrino and Calladine,[19] Motro et al.,[20] and Hanaor[21] have made important contributions toward further knowledge of the statics of these structures. Linear dynamic analysis results have been published by Motro et al.[20] and Furuya.[22] Nonlinear dynamics and control design studies have been reported by Skelton and Sultan[23] and Sultan and Skelton.[24] Applications of tensegrity structures are now being proposed, ranging from tensegrity domes (see Hanaor[25] and Wang and Liu[26]) to tensegrity sensors (Sultan and Skelton[27]) and space telescopes (Sultan et al.[28]).

In this paper, we design a nonlinear robust tracking controller for simulator motion control. The controller, which has been derived in Zenieh and Corless,[29] assures exponential convergence of the tracking error to a ball of prespecified radius, with a prespecified rate of convergence. This controller has two important advantages over other tracking controllers: It is a continuous controller, and it is simple to implement because it does not involve the computation of the regressor matrix.[30] It is a known fact that exact tracking usually results in discontinuous controllers that are undesirable for several reasons (see Corless[31]).

The paper is organized as follows. First a description of the proposed tensegrity simulator is given, followed by the derivation of its equations of motion. The statics of the simulator is analyzed and the equilibrium configurations are mathematically characterized. Next, the design of the nonlinear robust tracking controller is presented. The performance of the simulator equipped with this controller is then evaluated by simulating specific longitudinal motions of a symmetric aircraft.

Tensegrity Simulator

A perspective view of a two-stage tensegrity simulator is given in Fig. 1. The first stage consists of a base with three bars ($A_{i1}B_{i1}$, $i = 1, 2, 3$) rigidly attached (clamped) to it. The second stage consists of a cabin with three bars ($A_{i2}B_{i2}$, $i = 1, 2, 3$) clamped to it. Twelve tendons connect the end points of the bars. The six tendons characterized by $B_{i1}A_{j2}$ are classified as saddle tendons. The remaining six, $A_{i1}A_{j2}$ and $B_{i1}B_{j2}$, are called diagonal tendons. For mathematical modeling we assume that the tendons are massless and linear elastic, whereas the base, cabin, and bars are rigid.

For simplicity, the base and cabin triangles $A_{11}A_{21}A_{31}$ and $B_{12}B_{22}B_{32}$, respectively, are chosen to be congruent equilateral triangles. We also assume that all bars are identical and that they are connected to the base and cabin so that the angles made by their axes of symmetry with the perpendicular to triangle $A_{11}A_{21}A_{31}$ or $B_{12}B_{22}B_{32}$ are all equal; we call this angle δ and we restrict it to satisfy $0 < \delta < 90$ deg. For $\delta = 0$ the bars are orthogonal to the triangles and for $\delta = 90$ deg their axes of symmetry belong to the triangles. The angles made by the projections of the bars $A_{i1}B_{i1}$ ($i = 1, 2, 3$) onto the $A_{11}A_{21}A_{31}$ plane with the vector $\boldsymbol{A}_{11}\boldsymbol{A}_{31}$ are α, $\alpha + 240$, $\alpha + 120$, respectively (see Fig. 2 for the definitions of α and δ). Similarly the angles made by the projections of the bars $A_{i2}B_{i2}$ ($i = 1, 2, 3$) onto the $B_{12}B_{22}B_{32}$ plane with $\boldsymbol{B}_{12}\boldsymbol{B}_{32}$ are α, $\alpha + 240$, $\alpha + 120$, respectively.

As an inertial reference frame, we choose an orthonormal dextral set of vectors $\boldsymbol{e}_1, \boldsymbol{e}_2, \boldsymbol{e}_3$ with origin at the geometric center of triangle $A_{11}A_{21}A_{31}$. The vector $\boldsymbol{e}_3$ is orthogonal to this triangle, pointing upward, whereas $\boldsymbol{e}_1$ is parallel to $\boldsymbol{A}_{11}\boldsymbol{A}_{31}$. We introduce a reference frame $\boldsymbol{s}_1, \boldsymbol{s}_2, \boldsymbol{s}_3$, called the second-stage reference frame and fixed in this stage. Its origin is at the mass center of the second stage, which is assumed to coincide with the geometric center of triangle

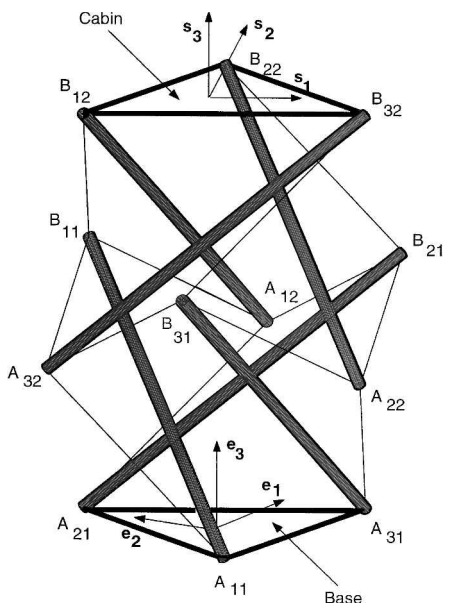

Fig. 1 Two-stage tensegrity simulator.

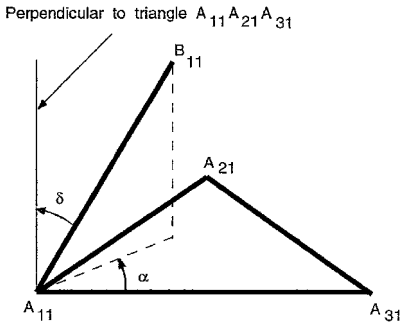

Fig. 2 Definition of α and δ.

$B_{12}B_{22}B_{32}$. The vector $\boldsymbol{s}_3$ is orthogonal to this triangle, pointing upward, whereas $\boldsymbol{s}_1$ is parallel to $\boldsymbol{B}_{12}\boldsymbol{B}_{32}$.

The simulator has six degrees of freedom. As independent generalized coordinates we choose ψ, ϕ, θ, the Euler angles for a 3-1-2 sequence to characterize the orientation of the second-stage reference frame relative to the inertial reference frame, and X, Y, Z, the Cartesian coordinates of the mass center of the second stage relative to the inertial reference frame. Thus, the vector $\boldsymbol{q}$ of generalized coordinates is given by

$$\boldsymbol{q} = [\psi \quad \phi \quad \theta \quad X \quad Y \quad Z]^T \tag{1}$$

Tensegrity Simulator Dynamics

The derivation of the second-order nonlinear ordinary differential equations that describe the dynamics of the tensegrity simulator, carried out using the Lagrange methodology, yields the following:

$$M(\boldsymbol{q})\ddot{\boldsymbol{q}} + \boldsymbol{c}(\boldsymbol{q}, \dot{\boldsymbol{q}}) + A(\boldsymbol{q})\boldsymbol{T}(\boldsymbol{q}) + \hat{\boldsymbol{G}} = 0 \tag{2}$$

The system inertia matrix $M(\boldsymbol{q})$ has the structure

$$M(\boldsymbol{q}) = \begin{bmatrix} \Omega^T J \Omega & 0 \\ 0 & M_t I \end{bmatrix} \tag{3}$$

where

$$\Omega = \begin{bmatrix} -\cos(\phi)\sin(\theta) & \cos(\theta) & 0 \\ \sin(\phi) & 0 & 1 \\ \cos(\phi)\cos(\theta) & \sin(\theta) & 0 \end{bmatrix}$$

The inertia matrix of the second stage J is calculated with respect to the second-stage reference frame. The components of the vector $\boldsymbol{c}(\boldsymbol{q}, \dot{\boldsymbol{q}})$ are quadratic functions of $\dot{\boldsymbol{q}}$ and are given by

$$c_i = \sum_{j=1}^{6}\sum_{m=1}^{6}\left(\frac{\partial M_{ij}}{\partial q_m} - \frac{1}{2}\frac{\partial M_{jm}}{\partial q_i}\right)\dot{q}_j\dot{q}_m \qquad \text{for} \qquad i = 1, \ldots, 6 \tag{4}$$

The vector $\boldsymbol{c}(\boldsymbol{q}, \dot{\boldsymbol{q}})$ can be expressed as

$$\boldsymbol{c}(\boldsymbol{q}, \dot{\boldsymbol{q}}) = C(\boldsymbol{q}, \dot{\boldsymbol{q}})\dot{\boldsymbol{q}} \tag{5}$$

The matrix $C(\boldsymbol{q}, \dot{\boldsymbol{q}})$ is not unique, however, if it is chosen according to

$$C_{ij} = \frac{1}{2}\sum_{m=1}^{6}\left(\frac{\partial M_{ij}}{\partial q_m} + \frac{\partial M_{im}}{\partial q_j} + \frac{\partial M_{jm}}{\partial q_i}\right)\dot{q}_m$$

$$\text{for} \qquad i = 1, \ldots, 6 \quad \text{and} \quad j = 1, \ldots, 6 \tag{6}$$

then the matrix $\dot{M}(\boldsymbol{q}) - 2C(q, \dot{q})$ is skew-symmetric. The vector $\boldsymbol{A}(\boldsymbol{q})\boldsymbol{T}(\boldsymbol{q})$ represents the generalized forces because of the tendons in tension, where $A_{mn} = \partial l_n / \partial q_m$ $(m = 1, \ldots, 6, n = 1, \ldots, 12)$ and $T_n = (k_n / l_{r_n})(l_n - l_{r_n})$ $(n = 1, \ldots, 12)$. The expressions for l_n are given in Appendix A. The vector $\hat{\boldsymbol{G}} = [0 \ 0 \ 0 \ 0 \ 0 \ M_t g]^T$ represents the generalized forces due to the gravitational forcefield.

Tensegrity Simulator Statics

Using Eq. (2), all equilibrium configurations $\boldsymbol{q}_g$ of the tensegrity simulator are given by

$$A(\boldsymbol{q}_g)\boldsymbol{T}(\boldsymbol{q}_g) + \hat{\boldsymbol{G}} = 0 \tag{7}$$

In addition all tendons should be in tension. Mathematically, this is characterized by

$$T_n(\boldsymbol{q}_g) > 0 \qquad \text{for} \qquad n = 1, \ldots, 12 \tag{8}$$

An equilibrium configuration in which all of the tendons are in tension is called a feasible equilibrium configuration. We are interested in feasible equilibrium configurations for which the cabin and base triangles are parallel and their mass centers are vertically aligned, i.e., $\boldsymbol{q}_g$ is given by

$$\boldsymbol{q}_g = [\psi_g \quad 0 \quad 0 \quad 0 \quad 0 \quad Z_g]^T \tag{9}$$

At a feasible configuration characterized by Eq. (9) the diagonal tendons $A_{i1}A_{j2}$ have the same length, D_1, the diagonal tendons $B_{i1}B_{j2}$ have the same length, D_2, the saddle tendons $B_{i1}A_{i2}$ have the same length, S_1, and the saddle tendons $B_{11}A_{32}$, $B_{21}A_{12}$, $B_{31}A_{22}$ have the same length, S_2. These lengths are given by

$$D_1 = \Big\{(2b^2/3)[1 + \cos(\psi_g - 60)] + h_g^2 + l^2 - 2lh_g\cos(\delta) + \left(2/\sqrt{3}\right)lb\sin(\delta)[\cos(\alpha + 30) + \sin(\psi_g - \alpha)]\Big\}^{\frac{1}{2}} \tag{10}$$

$$D_2 = \Big\{(2b^2/3)[1 - \cos(\psi_g)] + h_g^2 + l^2 - 2lh_g\cos(\delta) + \left(2/\sqrt{3}\right)lb\sin(\delta)[\cos(\psi_g - \alpha + 30) - \cos(\alpha - 30)]\Big\}^{\frac{1}{2}} \tag{11}$$

$$S_1 = \Big\{(2b^2/3)[1 + \cos(\psi_g - 60)] + h_g^2 + l^2\sin^2(\delta) + \left(2/\sqrt{3}\right)lb\sin(\delta)[\sin(\psi_g - \alpha - 60) - \sin(\alpha)]\Big\}^{\frac{1}{2}} \tag{12}$$

$$S_2 = \Big\{(2b^2/3)[1 - \cos(\psi_g)] + h_g^2 + l^2\sin^2(\delta) + \left(2/\sqrt{3}\right)lb\sin(\delta)[\sin(\alpha - 60) + \cos(\psi_g - \alpha - 30)]\Big\}^{\frac{1}{2}} \tag{13}$$

respectively. The overlap h_g, defined as the distance between triangles $A_{12}A_{22}A_{32}$ and $B_{11}B_{21}B_{31}$ and related to Z_g by $h_g = 2l\cos(\delta) - Z_g$, is positive $(h_g > 0)$ if the distance between $A_{12}A_{22}A_{32}$ and $A_{11}A_{21}A_{31}$ is smaller than the distance between $B_{11}B_{21}B_{31}$ and $A_{11}A_{21}A_{31}$.

For simplicity we assume that all tendons have the same stiffness k, all the diagonal tendons have the same rest-length D_r, and all the saddle tendons have the same rest-length S_r. Hence tensions in tendons of length D_1, D_2, S_1, S_2 are equal to

$$T_{D_1} = k(D_1 - D_r)/D_r, \qquad T_{D_2} = k(D_2 - D_r)/D_r$$
$$T_{S_1} = k(S_1 - S_r)/S_r, \qquad T_{S_2} = k(S_2 - S_r)/S_r \tag{14}$$

respectively.

The requirement that the feasible equilibrium configurations are characterized by Eq. (9) must hold for $\hat{\boldsymbol{G}}$ varying in a certain domain, i.e., the design should tolerate variations in the mass of the cabin. If we substitute Eq. (9) into Eqs. (7) and (8), we obtain the conditions these feasible equilibrium configurations must satisfy

$$A_g\boldsymbol{T}_g + [0 \quad M_t g]^T = 0$$
$$T_{D_1} > 0, \quad T_{D_2} > 0, \quad T_{S_1} > 0, \quad T_{S_2} > 0 \tag{15}$$

Here $\boldsymbol{T}_g = [T_{D_1} \ T_{D_2} \ T_{S_1} \ T_{S_2}]^T$ and A_g is a 2×4 matrix given in Appendix B. To solve these conditions for the feasible equilibrium configurations (ψ_g and Z_g), we have to choose the rest-lengths of the tendons. In the following we shall choose the rest-lengths of the tendons using certain feasible equilibrium configurations of the tensegrity structure, called prestressable configurations.

Prestressable Configurations

Consider the case when no gravity is present, i.e., $\hat{\boldsymbol{G}} = 0$. The corresponding feasible equilibrium configurations are called prestressable configurations. Let $\boldsymbol{q}_0$ denote a prestressable configuration. We impose the condition that at the equilibrium $\boldsymbol{q}_0$ the second stage is

obtained from the first through a clockwise rotation of 60 deg around the axis $\boldsymbol{e}_3$, i.e., $\psi_0 = 300$ deg and

$$\boldsymbol{q}_0 = [300 \quad 0 \quad 0 \quad 0 \quad 0 \quad Z_0] \tag{16}$$

With this geometry, all saddle and diagonal tendons have the same lengths given by

$$S_0 = \left\{h_0^2 + b^2/3 + l^2 \sin^2(\delta) - \left(2/\sqrt{3}\right) lb \sin(\delta)\cos(\alpha - 30)\right\}^{\frac{1}{2}} \tag{17}$$

$$D_0 = \left\{l^2 + b^2/3 + h_0^2 - 2lh_0\cos(\delta) - \left(2/\sqrt{3}\right) lb \sin(\delta)\sin(\alpha)\right\}^{\frac{1}{2}} \tag{18}$$

respectively. Here $h_0 = 2l\cos(\delta) - Z_0$ is the overlap in the prestressable configuration $\boldsymbol{q}_0$.

In this configuration, the tensions in the saddle and diagonal tendons are equal to T_S and T_D, respectively, hence the first condition in Eq. (15) reduces to

$$\begin{bmatrix} \cos(\alpha)/D_0 & \cos(\alpha + 60)/S_0 \\ [h_0 - l\cos(\delta)]/D_0 & h_0/S_0 \end{bmatrix} \begin{bmatrix} T_D \\ T_S \end{bmatrix} = 0 \tag{19}$$

The second of the preceding equations $(h_0 - l\cos(\delta))(T_D/D_0) + h_0(T_S/S_0) = 0$ and the condition that $0 < \delta < 90$ deg show that in order for the tensions to be positive ($T_D > 0$, $T_S > 0$), we must have

$$0 < h_0 < l\cos(\delta) \tag{20}$$

Equation (19) must hold for nonzero $[T_D \quad T_S]^T$, thus the determinant of the 2×2 matrix multiplying $[T_D \quad T_S]^T$ must be zero; this is equivalent to

$$h_0 = -\frac{l\cos(\delta)\cos(\alpha + 60)}{\cos(\alpha - 60)} \tag{21}$$

The constraint $0 < h_0 < l\cos(\delta)$ leads to 30 deg $< \alpha <$ 90 deg or 210 deg $< \alpha <$ 270 deg. Solving Eq. (19) for the tensions, we obtain that

$$T_S = PT_{0_S}, \qquad T_D = PT_{0_D} \tag{22}$$

where

$$\begin{bmatrix} T_{0_S} & T_{0_D} \end{bmatrix} = \frac{1}{\sqrt{6}} \begin{bmatrix} \dfrac{l\cos(\delta) - h_0}{h_0} & \dfrac{D_0}{S_0} \end{bmatrix} \times \frac{1}{\left\| \{[(l\cos(\delta) - h_0)/h_0](D_0/S_0)\} \right\|} \tag{23}$$

is a normalized vector such that the Euclidean norm of the vector $\boldsymbol{T}$ of all tensions is one for $P = 1$.

Using the expressions for the tensions T_S and T_D,

$$T_S = (k/S_r)(S_0 - S_r), \qquad T_D = (k/D_r)(D_0 - D_r) \tag{24}$$

we get the following expressions for S_r and D_r in terms of h_0 and P:

$$S_r = kS_0 \Big/ \left(T_{0_S} P + k\right), \qquad D_r = kD_0 \Big/ \left(T_{0_D} P + k\right) \tag{25}$$

An important issue in tensegrity structures research is the stability of the prestressable configurations.[16] It can be shown that for $(\alpha, \delta) \in (30, 90) \times (0, 90)$ the prestressable configurations previously analyzed are stable. Indeed, consider the potential energy of the structure in the absence of the gravitational field:

$$V = \sum_{n=1}^{12} \frac{k_n}{l_{r_n}} \left(l_n - l_{r_n}\right)^2 \tag{26}$$

The second derivative of the potential energy with respect to the generalized coordinates is given by

$$K_{ij} = \frac{\partial V}{\partial q_i \partial q_j}, \qquad i = 1, \ldots, 6, \qquad j = 1, \ldots, 6 \tag{27}$$

If we evaluate K at a prestressable configuration characterized by $q_0 = [300 \ 0 \ 0 \ 0 \ 0 \ 2l\cos(\delta) - h_0]$ with h_0 given by Eq. (21) and use the corresponding rest-lengths given by Eq. (25) we get

$$K_0 = \text{diag}[K_{11} \quad K_{11}/2 \quad K_{11}/2 \quad K_{44} \quad K_{44} \quad K_{44}] \tag{28}$$

where

$$K_{11} = 2b^2(T_S/S_0 + T_D/D_0) + 2\sqrt{3}lb \sin(\delta) \times [(T_S/S_0)\sin(\alpha + 60) + (T_D/D_0)\sin(\alpha)] \tag{29}$$

$$K_{44} = 12(T_S/S_0 + T_D/D_0) \tag{30}$$

For $(\alpha, \delta) \in (30, 90) \times (0, 90)$ and for $P > 0$ we have $K_{11} > 0$ and $K_{44} > 0$, yielding $K_0 > 0$, which proves that these prestressable configurations are stable.

For simulator design we choose the values of α and δ such that sufficient clearance between the bars is guaranteed. For this purpose we proceed as follows. Consider a pair (α, δ) and compute the minimum distance d_{ij}^{mn} between two bars $A_{ij}B_{ij}$ and $A_{mn}B_{mn}$. The problem of minimum distance between their axes of symmetry leads to a constrained quadratic optimization problem:

$$d_{ij}^{mn} = \min_w (w^T H w + f^T w + c), \qquad w = [w_1 \quad w_2] \qquad 0 \le w_{1,2} \le 1 \tag{31}$$

$$H = \begin{bmatrix} \|\boldsymbol{v}_1\|^2 & -\boldsymbol{v}_1 \cdot \boldsymbol{v}_2 \\ -\boldsymbol{v}_1 \cdot \boldsymbol{v}_2 & \|\boldsymbol{v}_2\|^2 \end{bmatrix}$$

$$f^T = [-2\boldsymbol{a} \cdot \boldsymbol{v}_1 \quad 2\boldsymbol{a} \cdot \boldsymbol{v}_2], \qquad c = \|\boldsymbol{a}\|^2 \tag{32}$$

where $\boldsymbol{a} = \boldsymbol{A}_{ij}\boldsymbol{A}_{mn}$, $\boldsymbol{v}_1 = \boldsymbol{A}_{ij}\boldsymbol{B}_{ij}$, $\boldsymbol{v}_2 = \boldsymbol{A}_{mn}\boldsymbol{B}_{mn}$.

We denote by $d(\alpha, \delta)$ the minimum of d_{ij}^{mn} over all possible combinations of bars, i.e., over all (i, j), (m, n) pairs $[i = 1, 2, 3, \ j = 1, 2, m = 1, 2, 3, \ n = 1, 2, (i, j) \neq (m, n)]$. Following this analysis we choose $\alpha = \delta = 60$ deg that, for $l = 5$ m, $b = 3.33$ m, yields a clearance $d(\alpha, \delta) = 1.2$ m. This procedure assumes that the prestressable configuration and the actual equilibrium configuration (when the gravitational field is acting) do not differ too much.

Feasible Equilibrium Configurations

The feasible equilibrium configurations of interest are characterized by Eqs. (15). We assume that the rest-lengths of the tendons are given by Eq. (25). For $M_t = 0$, $G = M_t g = 0$ and we know that Eqs. (15) have a solution; thus we expect them to have a solution for small $M_t \neq 0$. A continuation procedure can be applied to solve for these solutions as follows: slightly increase M_t and solve the two nonlinear equations $A_g \boldsymbol{T}_g + [0 \ M_t g]^T = 0$ for ψ_g and h_g (using classical nonlinear solvers like Newton–Raphson), then check if $T_{g_i} > 0$ $(i = 1, \ldots, 4)$. If this happens, then we have found a new feasible equilibrium configuration with $\boldsymbol{q}_g = [\psi_g \ 0 \ 0 \ 0 \ 0 \ Z_g]^T$ where $Z_g = 2l\cos(\delta) - h_g$. We continue to increase M_t and repeat the procedure until one of the tendons becomes slack or when the M_t of interest is reached. To illustrate the application of this procedure, a graph of the variation of ψ_g and Z_g with the mass of the second stage (top), M_t, is given in Fig. 3 for the following characteristics:

$$l = 5 \text{ m}, \qquad b = 3.33 \text{ m}, \qquad \alpha = 60 \text{ deg}, \qquad \delta = 60 \text{ deg}$$

$$P = 2000, \qquad k = 5000 \text{ N}, \qquad g = 9.81 \text{ m s}^{-2} \tag{33}$$

At all points on these curves the distances between bars were computed to ascertain if the bars intersect. This did not happen (the minimum distance between two bars was 0.7 m).

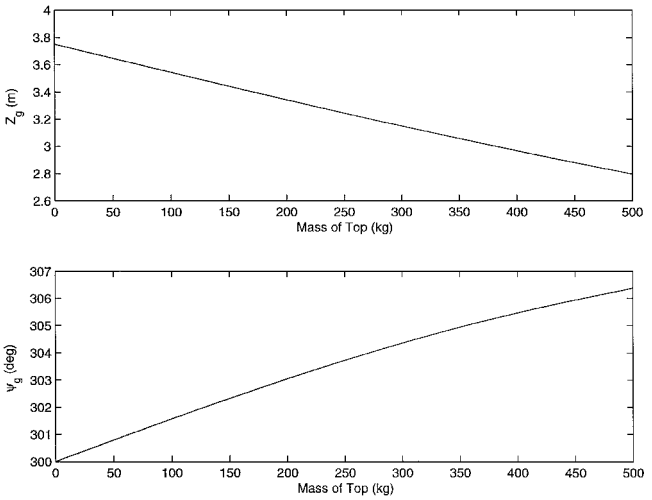

Fig. 3 Variation of ψ_g and Z_g with mass of second stage.

Robust Tracking Controller

The control inputs for the simulator are the rest-lengths of some of the tendons. For further analysis, we separate the tendons into active tendons of controlled rest-lengths and passive tendons of fixed rest-lengths. Using Eqs. (2) and (5), the behavior of the simulator is described by

$$M(\boldsymbol{q})\ddot{\boldsymbol{q}} + C(\boldsymbol{q}, \dot{\boldsymbol{q}})\dot{\boldsymbol{q}} + A^p(\boldsymbol{q})\boldsymbol{T}^p(\boldsymbol{q}) + A^a(\boldsymbol{q})\boldsymbol{T}^a + \hat{\boldsymbol{G}} = 0 \qquad (34)$$

where the components of $\boldsymbol{T}^p$ and $\boldsymbol{T}^a$ are the tensions in the passive and active tendons, respectively.

For robust control design we consider that the mass of the second stage may be uncertain. The uncertainty is represented by the lumped uncertain term $\mu \in \Delta$, where Δ is a known nonempty set. Thus the equations of motion transform to

$$M(\boldsymbol{q}, \mu)\ddot{\boldsymbol{q}} + C(\boldsymbol{q}, \dot{\boldsymbol{q}}, \mu)\dot{\boldsymbol{q}} + A^p(\boldsymbol{q})\boldsymbol{T}^p(\boldsymbol{q}) + A^a(\boldsymbol{q})\boldsymbol{T}^a + \hat{\boldsymbol{G}}(\mu) = 0 \qquad (35)$$

For further analysis we write the equations of motion as

$$M(\boldsymbol{q}, \mu)\ddot{\boldsymbol{q}} + C(\boldsymbol{q}, \dot{\boldsymbol{q}}, \mu)\dot{\boldsymbol{q}} + \boldsymbol{u}_0 + A^p(\boldsymbol{q})\boldsymbol{T}^p(\boldsymbol{q}) + \hat{\boldsymbol{G}}(\mu) = \boldsymbol{u} \qquad (36)$$

where

$$\boldsymbol{u} = -A^a(\boldsymbol{q})\boldsymbol{T}^a + \boldsymbol{u}_0, \qquad \boldsymbol{u}_0 = A^a(\boldsymbol{q}_g)\boldsymbol{T}^a(\boldsymbol{q}_g) \qquad (37)$$

Here $\boldsymbol{q}_g$ is a feasible equilibrium configuration. Under the assumption of invertibility of $A^a(\boldsymbol{q})$, Eq. (37) can be solved for the active rest-lengths $l^a_{r_1}, \ldots, l^a_{r_{n_u}}$; specifically,

$$l^a_{r_i} = \frac{k^a_i l^a_i}{k^a_i + T^a_i} \qquad \text{for} \qquad i = 1, \ldots, n_u \qquad (38)$$

where $\boldsymbol{T}^a$, the vector of active tensions, is given by $\boldsymbol{T}^a = A^a(q)^{-1}(\boldsymbol{u}_0 - \boldsymbol{u})$.

The issue of active tendon selection is addressed next. Because the number of generalized coordinates is six, the system will be controlled with six tendons. The six are chosen by analyzing the properties of the matrix $A(\boldsymbol{q}_g)$. Specifically, we consider the set of all matrices created by combining any six columns of $A(\boldsymbol{q}_g)$; let these matrices be denoted by A_i $(i = 1, \ldots, 924)$. We compute the corresponding set of minimum singular values $\sigma_i = \sigma_{\min}(A_i)$ $(i = 1, \ldots, 924)$. The A_i, which yields the maximum of $\{\sigma_i, i = 1, \ldots, 924\}$, provides the set of active tendons. Applying this procedure with the data in Eqs. (33) and with $\boldsymbol{q}_g$ corresponding to the nominal mass $M_t = 140$ kg of the simulator, we obtain that the set of saddle tendons is the best choice for the set of active tendons.

Let $\boldsymbol{q}^d(\cdot) : \mathbb{R} \to \mathbb{R}^6$ be a desired motion of the simulator. Ideally, we wish to design a controller such that every motion $\boldsymbol{q}(\cdot) : \mathbb{R} \to \mathbb{R}^6$ of the closed-loop system converges to the desired motion exponentially. We also want to specify the rate of convergence γ a priori. The requirement that the tracking error $\tilde{\boldsymbol{q}} = \boldsymbol{q} - \boldsymbol{q}^d$ converges to zero usually leads to a discontinuous controller that is undesirable for several reasons (see Corless[31]). However, if we only require tracking to within some prespecified tolerance r we can design a continuous controller (see Zenieh and Corless[29]). Specifically, given r, $\gamma > 0$, we can design a controller so that the closed-loop system is a *robust $r - \gamma$ tracker*; namely, there exists scalars c_1 and c_2 such that, for any desired (twice continuously differentiable) trajectory $\boldsymbol{q}^d(\cdot)$ and any uncertainty $\mu \in \Delta$ every solution satisfies

$$\|\tilde{\boldsymbol{q}}(t)\| \le (c_1\|\tilde{\boldsymbol{q}}(t_0)\| + c_2\|\dot{\tilde{\boldsymbol{q}}}(t_0)\|)\exp(-\gamma(t - t_0)) + r \qquad \text{for} \quad t \ge t_0 \qquad (39)$$

which means that the tracking error exponentially converges with rate γ to the ball of radius r defined by $\|\tilde{\boldsymbol{q}}\| \le r$.

To apply the results of Zenieh and Corless[29] for controller design, it is assumed that there exists positive constants $\beta_0, \beta_1, \beta_2, \beta_3$, such that for all $\boldsymbol{q}$, $\dot{\boldsymbol{q}}$, and μ,

$$0 < \beta_0 I \le M(\boldsymbol{q}, \mu) \le \beta_1 I, \qquad \|C(\boldsymbol{q}, \dot{\boldsymbol{q}}, \mu)\| \le \beta_2\|\dot{\boldsymbol{q}}\|$$

$$\|\boldsymbol{u}_0 + A^p(\boldsymbol{q})\boldsymbol{T}^p(\boldsymbol{q}) + \hat{\boldsymbol{G}}(\mu)\| \le \beta_3 \qquad (40)$$

If we express $C(\boldsymbol{q}, \dot{\boldsymbol{q}}, \mu)$ as $C(\boldsymbol{q}, \dot{\boldsymbol{q}}, \mu) = \mathrm{diag}(\dot{\boldsymbol{q}}^T)\tilde{C}(\boldsymbol{q}, \mu)$ we get $\|C(\boldsymbol{q}, \dot{\boldsymbol{q}}, \mu)\| \le \|\tilde{C}(\boldsymbol{q}, \mu)\|\|\dot{\boldsymbol{q}}\|$. Thus β_2 can be chosen to an upper bound on the maximum singular value of $\tilde{C}(\boldsymbol{q}, \mu)$.

Because analytical determination of the bounds $\beta_0, \beta_1, \beta_2, \beta_3$ is not usually possible, they are numerically determined. One approach is to discretize the problem by gridding Δ and the domain $\mathcal{D}$ in the space of generalized coordinates in which it is reasonable to assume that the system trajectories lie. Let $(\boldsymbol{q}_i, \mu_i)$ $(i = 1, \ldots, N)$ denote N grid points. We evaluate the minimum and maximum eigenvalues of $M(\boldsymbol{q}_i, \mu_i)$ (called $\lambda_{\min_i}$ and $\lambda_{\max_i}$, respectively), the maximum singular value of $\tilde{C}(\boldsymbol{q}_i, \mu_i)$ (called $\sigma_{\max_i}$), and the quantity $F_i = \|\boldsymbol{u}_0 + A^p(\boldsymbol{q}_i)\boldsymbol{T}^p(\boldsymbol{q}_i) + \hat{\boldsymbol{G}}(\mu_i)\|$. Any positive number smaller than the minimum of $\{\lambda_{\min_i}, i = 1, \ldots, N\}$ can be chosen as β_0, whereas any number greater than the maximum of $\{\lambda_{\max_i}, i = 1, \ldots, N\}$ can be chosen as β_1. Similarly any number greater than the maximum of $\{\sigma_{\max_i}, i = 1, \ldots, N\}$ can be chosen as β_2 and a number greater than the maximum of $\{F_i, i = 1, \ldots, N\}$ can be chosen as β_3. A finer grid can be used to test if the chosen values are satisfactory.

In Zenieh and Corless[29] the following nonlinear, continuous controller has been proposed for robust tracking control of a general class of mechanical systems:

$$\boldsymbol{u} = -Q\eta - (\|\rho\eta\| + \epsilon)^{-1}\rho^2\eta, \qquad \rho = \beta_1\|\dot{\nu}\| + \beta_2\|\nu\| + \beta_3$$

$$\nu = \dot{\boldsymbol{q}}^d - \Lambda\tilde{\boldsymbol{q}}, \qquad \eta = \dot{\tilde{\boldsymbol{q}}} + \Lambda\tilde{\boldsymbol{q}} \qquad (41)$$

Here Q, Λ, and ϵ satisfy

$$Q > \gamma\beta_1 I, \qquad 0 < \epsilon \le (\gamma r)^2\lambda_{\min}(Q)(\beta_0/\beta_1), \qquad \lambda > \gamma I \qquad (42)$$

where $\lambda_{\min}(Q)$ denotes the minimum eigenvalue of the positive-definite symmetric matrix Q.

The resulting closed-loop system has been shown to be a robust $r - \gamma$ tracker with

$$c_1 = 1 + \lambda_{\max}(\Lambda)c_2, \qquad c_2 = \beta_1/\beta_0(\gamma_1 - \gamma)$$

$$\gamma_1 = \lambda_{\min}(Q)/\beta_1 \qquad (43)$$

where $\lambda_{\max}(\Lambda)$ is the maximum eigenvalue of the positive-definite symmetric matrix Λ (see Zenieh and Corless[29]).

Simulating Longitudinal Motions of a Symmetric Aircraft

In flight simulation, the desired motion $\boldsymbol{q}^d(\cdot)$ to be tracked by the simulator is generated by the motion of an aircraft. We consider here the longitudinal motion of a symmetric aircraft. A longitudinal motion of a symmetric aircraft can occur when the resultant force belongs to the longitudinal plane of symmetry of the aircraft and

the resultant torque is orthogonal to it. Using a single rigid-body model to describe the longitudinal motion of a symmetric aircraft and assuming no wind, the following equations of motion can be derived through the application of the laws of mechanics:

$$\dot{X}_a = v\cos(\theta_a - \alpha_a), \qquad \dot{Z}_a = -v\sin(\theta_a - \alpha_a), \qquad \dot{\theta}_a = \omega_y$$

$$m_a\dot{v} = T_r\cos\alpha_a - D - m_a g\,\sin(\theta_a - \alpha_a)$$

$$m_a v\dot{\alpha}_a = -T_r\sin\alpha_a - L + m_a g\cos(\theta_a - \alpha_a) + m_a v\omega_y$$

$$J_a\dot{\omega}_y = M_y \tag{44}$$

The horizontal range (X_a) and the altitude (Z_a) of the aircraft are measured with respect to a dextral set of unit vectors $\boldsymbol{f}_1, \boldsymbol{f}_2, \boldsymbol{f}_3$, attached to the Earth. The motion is assumed to take place in the vertical $\boldsymbol{f}_1 - \boldsymbol{f}_3$ plane with $\boldsymbol{f}_3$ vertical. In this model, we neglect the gyroscopic couples (because of rotating rigid bodies) as well as a propulsion contribution to the pitching moment (because of offset of the resultant thrust from the aircraft center of mass). For simulator design we shall use the vector $\boldsymbol{q}_a$ of generalized coordinates of the aircraft defined by

$$\boldsymbol{q}_a = [\psi_a \quad \phi_a \quad \theta_a \quad X_a \quad Y_a \quad Z_a]^T \tag{45}$$

By the choice of the inertial reference frame attached to the Earth, the aircraft motion takes place in a vertical plane and we have $\psi_a = \phi_a = Y_a = 0$.

The aerodynamic forces L, D, and the pitching moment M_y are given by

$$L = \left(\rho_a S v^2/2\right)C_l, \qquad D = \left(\rho_a S v^2/2\right)C_d$$

$$M_y = \left(\rho_a S v^2\tilde{c}/2\right)C_M \tag{46}$$

For small variations of the Mach number, the aerodynamic coefficients can be considered independent of this parameter. For a certain aircraft, whose dynamic properties are analyzed in Sultan,[32] these coefficients depend on α_a, δ_e, and δ_f, and are given in Appendix C. The atmosphere model used here yields the following dependency of the air density ρ_a on the altitude Z_a:

$$\rho_a = 1.22625\exp[4.256\log(1 - Z_a/44300)]\ \text{kg m}^{-3} \tag{47}$$

where Z_a is given in meters.

Evaluation of the Tensegrity Simulator

In the following we analyze the ability of the tensegrity simulator to track longitudinal motions of an aircraft. First we define what we mean by tracking and desired motion in this context.

The main task of a flight simulator is to give the pilot the same sensations one would have when flying the real aircraft. In the first approximation we neglect the influence of the vestibular system of the pilot. For simplicity we also assume that the pilot's head location with respect to the mass center of the second stage of the simulator is the same as its location would be with respect to the mass center of the aircraft. Thus, in case the simulator tracks reasonably well the acceleration and angular velocity of the aircraft, the pilot will have the same sensations when flying the simulator as when flying the real aircraft.

Mathematically, the tracking problem means that the simulator and the aircraft should have the same accelerations and angular velocities. Usually, they start from different initial configurations and velocities. The simulator is in equilibrium with zero velocity, which is dynamically equivalent to a rectilinear uniform translation of the aircraft at an arbitrary velocity. It is sufficient for the simulator to track the aircraft motion because of a certain command as seen from an inertial reference frame attached to the aircraft that is in rectilinear uniform motion before the command is applied. Thus the desired motion is given by

$$\boldsymbol{q}^d(t) = \boldsymbol{q}_a(t) - \dot{\boldsymbol{q}}_{a_0}t - \boldsymbol{q}_{a_0} + \boldsymbol{q}_0 + \dot{\boldsymbol{q}}_0 t \tag{48}$$

where q_0, $\dot{q}_0$, q_{a_0}, $\dot{q}_{a_0}$ are the initial conditions of the simulator and aircraft (usually $\dot{\boldsymbol{q}}_0 = 0$). In this paper we are mainly interested in the capability of the tensegrity simulator equipped with the nonlinear robust tracking controller to track the desired motion at the onset of the acceleration, i.e., immediately after an aerodynamic or throttle command is applied.

We now consider the following scenario. The aircraft is in uniform rectilinear translation; correspondingly, the simulator is in equilibrium, characterized by $\boldsymbol{q}_g$. Then, a command that does not take the aircraft out of its longitudinal flight is performed. As a result the simulator should undergo a motion to track the desired trajectory:

$$\boldsymbol{q}^d = [\psi_g \quad 0 \quad \theta^d \quad X^d \quad 0 \quad Z^d]^T \tag{49}$$

where

$$\theta^d = \theta_a - \theta_{a_0}, \qquad X^d = X_a - \dot{X}_{a_0}t - X_{a_0}$$

$$Z^d = Z_a - \dot{Z}_{a_0}t - Z_{a_0} + Z_g \tag{50}$$

For simplicity we assume that the second-stage reference frame is central principal for the second stage such that its inertia matrix J is diagonal, $J = \text{diag}[J_1 \ \ J_2 \ \ J_3]$. We choose the following nominal inertial parameters for the simulator:

$$M_t = 140\ \text{kg}, \qquad J_1 = 300\ \text{kg m}^2$$

$$J_2 = 400\ \text{kg m}^2, \qquad J_3 = 500\ \text{kg m}^2 \tag{51}$$

The geometric and elastic parameters are those given in Eqs. (33). The controller is designed using the following parameters:

$$\gamma = 25, \quad r = 0.2, \quad \beta_0 = 90, \quad \beta_1 = 700, \quad \beta_2 = 500$$

$$\beta_3 = 40000, \quad \epsilon = 56252, \quad \Lambda = 26I, \quad Q = 17501I \tag{52}$$

The bounds β_i ($i = 0, 1, 2, 3$) have been determined based on a grid of the set $\mathcal{D} \times \Delta$ where $\Delta = [90, 190]$ kg and

$$\mathcal{D} = [\psi_g - 30, \psi_g + 30] \times [-30, 30] \times [-30, 30]$$
$$\times [-b/3, b/3] \times [-b/3, b/3]$$
$$\times [Z_g - b/3, Z_g + b/3]$$

Here ψ_g and Z_g are the nominal values (corresponding to $M_t = 140$ kg) of ψ and Z at equilibrium. The increments used in gridding were 5 deg for ψ, ϕ, and θ, $b/6$ for X, Y, Z, and 2 kg for $\mu = M_t$.

The mass of the aircraft is $m_a = 1400$ kg and the pitching moment of inertia is $J_a = 60{,}000$ kg m^2. The lifting surface is $S = 11.9$ m^2 and the mean aerodynamic chord is $\tilde{c} = 1.22$ m.

Elevator Command

Here we evaluate the ability of the system to simulate the motion of the aircraft when subjected to an elevator step input command. Assume that the aircraft is initially in level flight characterized by the following trim conditions:

$$Z_{a_0} = 3000\ \text{m}, \quad \theta_{a_0} = 0, \quad \alpha_{a_0} = 0, \quad \dot{X}_{a_0} = 86.4\ \text{m s}^{-1}$$
$$\delta_{f_0} = 0, \quad \delta_{e_0} = -1.34\ \text{deg}, \quad T_{r_0} = 1479\ \text{N} \tag{53}$$

The corresponding simulator equilibrium is characterized by

$$\psi_g = 302.2\ \text{deg}, \quad Z_g = 3.46\ \text{m}, \quad X = Y = \phi = \theta = 0 \tag{54}$$

The elevator, which is approximated as a first-order system with time constant $\tau = 0.2$ s, is given a step command at time $t_0 = 0.5$ s. This results in the elevator deflection,

$$\delta_e = \delta_{e_0} + \delta_e^A\{1 - \exp[-(t - t_0)/\tau]\} \tag{55}$$

We present next the time histories of the most significant accelerations (Fig. 4), the control inputs (Fig. 5), and the actuator forces (Fig. 6) for $\delta_e^A = 2$ deg. The following notation has been introduced for the tendons: tendon $1 = A_{12}B_{21}$, $2 = A_{12}B_{11}$, $3 = A_{22}B_{21}$, $4 = A_{22}B_{31}$, $5 = A_{32}B_{11}$, $6 = A_{32}B_{31}$.

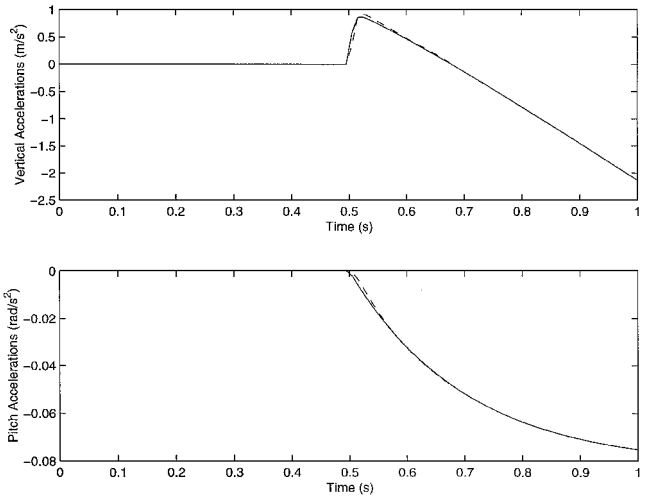

Fig. 4 Elevator command: desired (——) and simulator (– – –) accelerations.

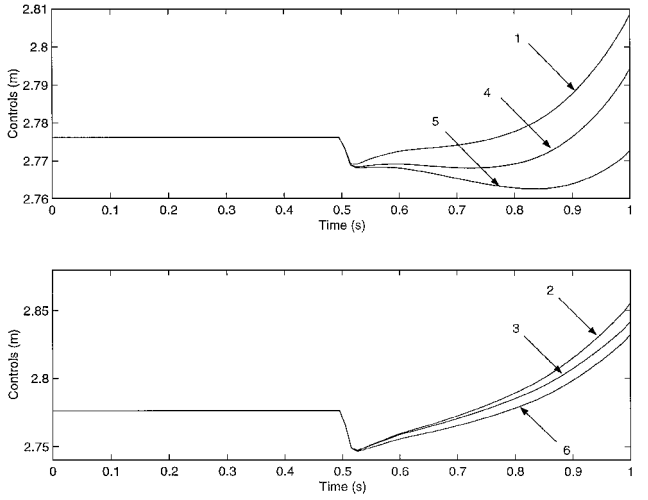

Fig. 5 Elevator command: control time histories.

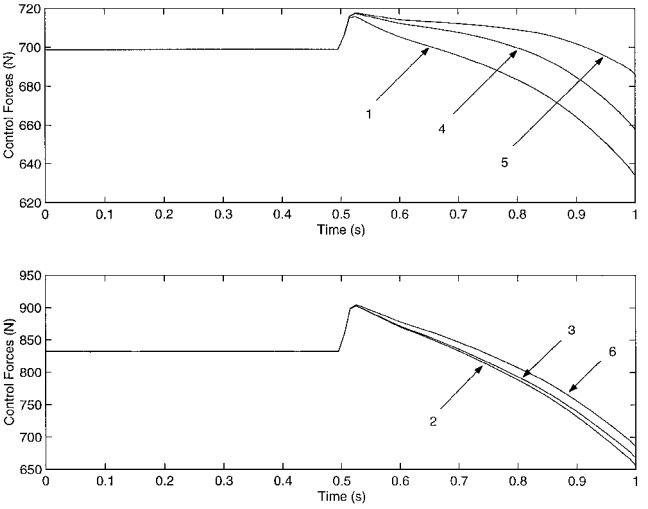

Fig. 6 Elevator command: actuator force time histories.

The simulator is very effective in tracking the accelerations even throughout the initial phase. Numerical simulations indicate that even better tracking is achieved for the generalized coordinates and velocities and for the angular velocity of the aircraft. The time histories of the control inputs and actuator forces show that their variations and ranges are acceptable. The simulations show that throughout the motion none of the tendons becomes slack, and there is always sufficient clearance between bars.

Flap Command

Here we evaluate the ability of the system to simulate the motion of the aircraft because of a flap step input command. Assume that the aircraft is initially in level flight characterized by

$$Z_{a_0} = 100 \text{ m}, \qquad \theta_{a_0} = 0, \qquad \alpha_{a_0} = 0, \qquad \dot{X}_{a_0} = 74.8 \text{ m s}^{-1}$$
$$\delta_{f_0} = 0, \qquad \delta_{e_0} = -1.34 \text{ deg}, \qquad T_{r_0} = 1479 \text{ N} \qquad (56)$$

and that approaching landing the flaps are given a deflection,

$$\delta_f = \delta_{f_0} + \delta_f^A\{1 - \exp[-(t - t_0)/\tau]\} \qquad (57)$$

with $\delta_f^A = 5$ deg, $t_0 = 0.5$ s, and $\tau = 0.5$ s. The equilibrium configuration of the simulator is the same as before.

Numerical simulations (Fig. 7) show that the simulator is very effective in tracking the accelerations. As in the elevator step command case, numerical simulations indicate that even better tracking is achieved for the generalized coordinates, generalized velocities, and angular velocity of the aircraft, although none of the tendons becomes slack and sufficient clearance between bars is guaranteed. The corresponding control input time histories, given in Fig. 8, show that their variations and ranges are acceptable (the same is true of the control forces).

Throttle Command

Finally, we evaluate the ability of the system to simulate the motion of the aircraft when subjected to a throttle step input command. We suppose that the aircraft is initially in level flight characterized

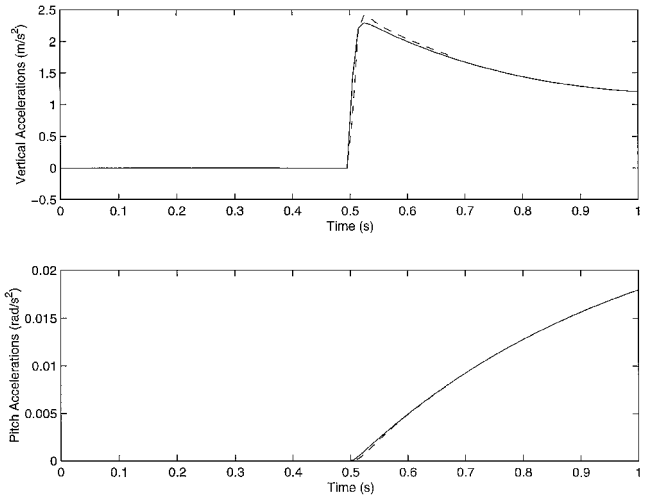

Fig. 7 Flap command: desired (——) and simulator (– – –) accelerations.

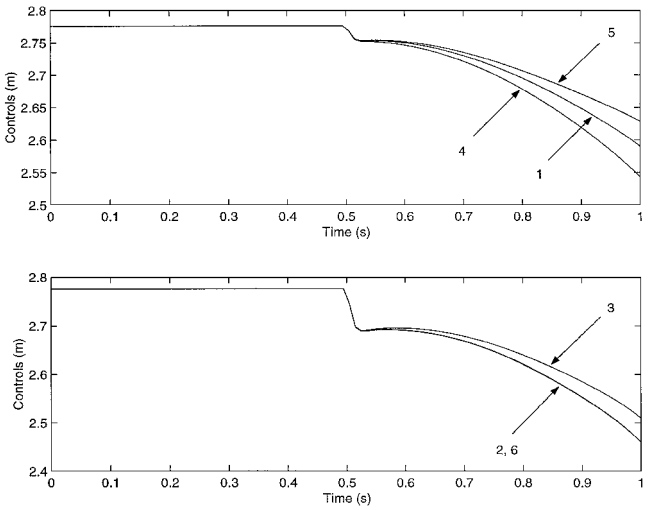

Fig. 8 Flap command: control time histories.

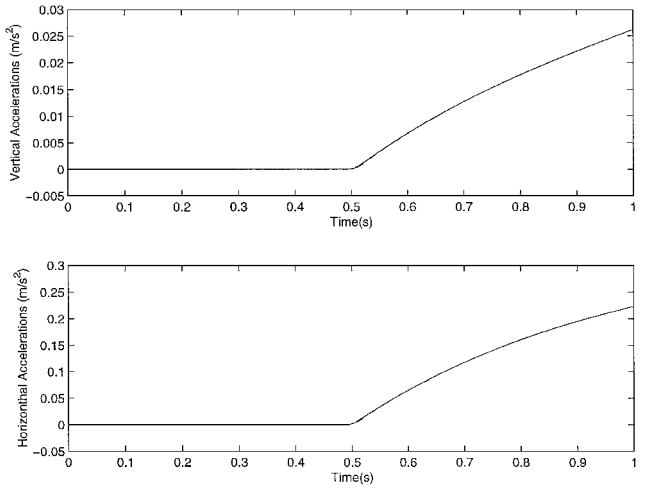

Fig. 9 Throttle command: desired (——) and simulator (– – –) accelerations.

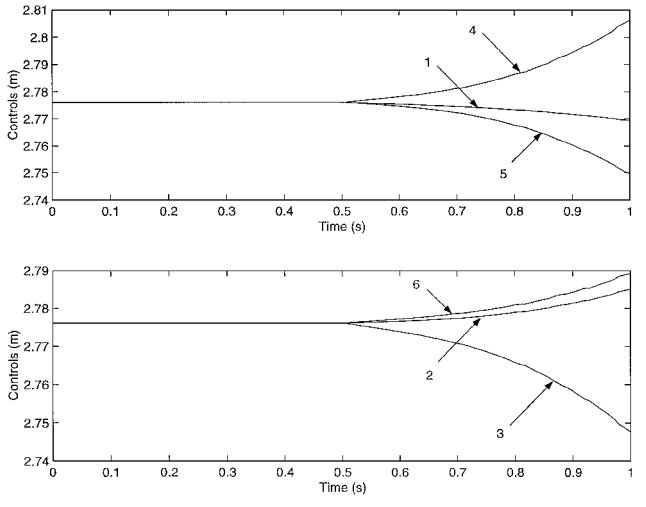

Fig. 10 Throttle command: control time histories.

by the parameters of the previous section and is given the throttle command,

$$T_r = T_{r_0} + T_r^A\{1 - \exp[-(t - t_0)/\tau]\} \tag{58}$$

with $T_r^A = 500$ N, $t_0 = 0.5$ s, and $\tau = 0.5$ s. The time histories of the significant accelerations and the controls are given in Figs. 9 and 10, respectively.

As in the case of the aerodynamic commands, tracking is very good, and none of the tendons becomes slack and there is sufficient clearance between bars. Here the control time histories exhibit smoother variations than in the case of the aerodynamic commands.

Robustness of the Design

In the following we evaluate the robustness of our design. We consider that the controller is designed for the nominal simulator, whose inertial properties are $M_t = 140$ kg, $J_1 = 300$ kg m^2, $J_2 = 400$ kg m^2, $J_3 = 500$ kg m^2, and that it is used to control the motion of the simulator when its inertial properties change.

For illustration, we consider an elevator step command with $\delta_e^A = 5$ deg, $t_0 = 0.5$ s, $\tau = 0.2$ s applied to the aircraft, which is initially in level flight characterized by the parameters in the subsection Elevator Command. Figure 11 shows the vertical acceleration of the aircraft and the corresponding vertical accelerations of three simulators: the nominal one and two perturbed simulators, whose inertial properties are varied between +50% and −50%, respectively, from the nominal ones (this means that the values of M_t, J_1, J_2, J_3 are varied between +50% and −50%, respectively, from the nominal ones). The response of the perturbed simulator whose inertial properties are varied +50% is represented in Fig. 11 by +, whereas the

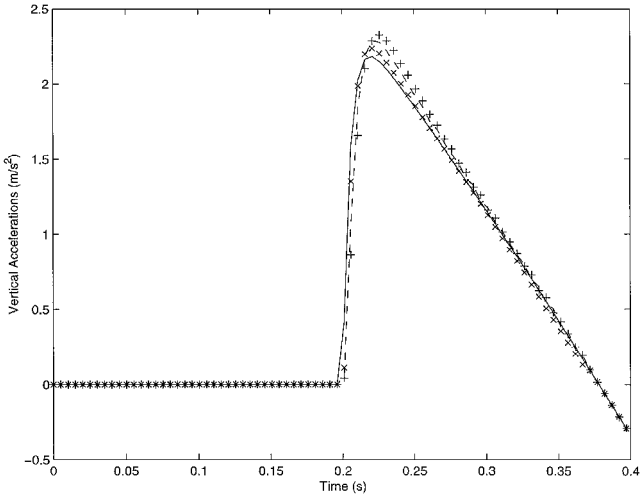

Fig. 11 Robustness evaluation: desired (——), nominal (– – –), and perturbed (+, ×) simulators.

response of the one whose inertial properties are varied with −50% is represented by ×. We ascertain that, even for these large perturbations in the inertial properties, the tracking is very good. The perturbed simulators responses are very close to the response of the nominal simulator and to the one of the aircraft. Our simulations confirm that even better tracking is obtained for the generalized coordinates and velocities while none of the tendons become slack and none of the bars touch each other.

It is also important to mention that, even though for controller design we assumed variations only in the mass of the cabin M_t, the design is very robust with respect to variations in all inertial parameters of the simulator. We also remark that the perturbed simulators masses considered in the preceding example are out of the range used for controller design ($\Delta = [90, 190]$ kg). However the perturbed simulators equipped with the nominal controller track the desired motion very well.

Conclusions

Motivated by the desire to eliminate complicated strut actuators, a tensegrity motion simulator is proposed. The main advantage that a tensegrity motion simulator has over a Stewart platform based simulator is that it does not have telescopic struts. Tensegrity simulators do not include rigid bodies sliding with respect to each other, nor do they have complicated bar to bar joints. The actuating and the sensing functions can be carried by the tendons.

For the proposed simulator, a nonlinear continuous robust tracking controller is designed. The controller guarantees exponential convergence of the tracking error—with a prespecified rate of convergence—to a ball of a prescribed radius. The physical controls are the rest-lengths of six of the 12 tendons of the tensegrity structure.

The proposed tensegrity simulator equipped with the robust tracking controller is very effective in tracking the longitudinal symmetric motions of a certain aircraft. In general, the motions generated by throttle commands are better tracked than those due to aerodynamic control surfaces commands. Further numerical simulations indicated that the design is very robust to variations in the inertial properties of the cabin.

Appendix A: Tendon Lengths

The lengths of the tendons l_j ($j = 1, \ldots, 12$) are given by

$$l_1 = \Big\{\Big[q_5 - A_2 - \big(b\sqrt{3}/6\big)\cos(q_1)\cos(q_2) - b\sqrt{3}/3 + l\sin(\delta)\sin(\alpha)\Big]^2 + \Big[q_4 - A_1 + \big(b\sqrt{3}/6\big)\sin(q_1)\cos(q_2) + l\sin(\delta)\cos(\alpha)\Big]^2 + \Big[q_6 + (b/2)\cos(q_2)\sin(q_3) - \big(b\sqrt{3}/6\big)\sin(q_2) - 2l\cos(\delta)\Big]^2\Big\}^{\frac{1}{2}}$$

$$l_2 = \Big\{\Big[q_4 - A_1 + \big(b\sqrt{3}/6\big)\sin(q_1)\cos(q_2) + l\sin(\delta)\sin(\alpha - 30) + b/2\Big]^2 + [q_5 - A_2 + A_3 - l\sin(\delta)\cos(\alpha - 30)]^2 + \Big[q_6 + (b/2)\cos(q_2)\sin(q_3) - \big(b\sqrt{3}/6\big)\sin(q_2) - 2l\cos(\delta)\Big]^2\Big\}^{\frac{1}{2}}$$

$$l_3 = \Big\{\Big[q_4 - \big(b\sqrt{3}/3\big)\sin(q_1)\cos(q_2) - l\sin(\delta)\cos(\alpha - 60)\Big]^2 + [q_5 - 2A_3 - l\sin(\delta)\sin(\alpha - 60)]^2 + \Big[q_6 + \big(b\sqrt{3}/3\big)\sin(q_2) - 2l\cos(\delta)\Big]^2\Big\}^{\frac{1}{2}}$$

$$l_4 = \Big\{\Big[q_4 - \big(b\sqrt{3}/3\big)\sin(q_1)\cos(q_2) - b/2 + l\sin(\delta)\sin(\alpha - 30)\Big]^2 + \Big[q_6 + \big(b\sqrt{3}/3\big)\sin(q_2) - 2l\cos(\delta)\Big]^2 + \Big[q_5 + \big(b\sqrt{3}/6\big)\cos(q_1)\cos(q_2) + b\sqrt{3}/6 - l\sin(\delta)\cos(\alpha - 30)\Big]^2\Big\}^{\frac{1}{2}}$$

$$l_5 = \Big\{\Big[q_4 + A_1 + \big(b\sqrt{3}/6\big)\sin(q_1)\cos(q_2) - l\sin(\delta)\cos(\alpha - 60) + b/2\Big]^2 + [q_5 + A_2 + A_3 - l\sin(\delta)\sin(\alpha - 60)]^2 + \Big[q_6 - (b/2)\cos(q_2)\sin(q_3) - \big(b\sqrt{3}/6\big)\sin(q_2) - 2l\cos(\delta)\Big]^2\Big\}^{\frac{1}{2}}$$

$$l_6 = \Big\{\Big[q_5 + A_2 - \big(b\sqrt{3}/6\big)\cos(q_1)\cos(q_2) + l\sin(\delta)\sin(\alpha) + b\sqrt{3}/6\Big]^2 + \Big[q_4 + A_1 + \big(b\sqrt{3}/6\big)\sin(q_1)\cos(q_2) + l\sin(\delta)\cos(\alpha) - b/2\Big]^2 + \Big[q_6 - b/2\cos(q_2)\sin(q_3) - \big(b\sqrt{3}/6\big)\sin(q_2) - 2l\cos(\delta)\Big]^2\Big\}^{\frac{1}{2}}$$

$$l_7 = \Big\{\Big[b/2 + q_4 + A_1 + \big(b\sqrt{3}/6\big)\sin(q_1)\cos(q_2) + l\sin(\delta) \times \cos(\alpha + 60)\Big]^2 + [A_3 + q_5 + A_2 + l\sin(\delta)\sin(\alpha + 60)]^2 + \Big[q_6 - (b/2)\cos(q_2)\sin(q_3) - \big(b\sqrt{3}/6\big)\sin(q_2) - l\cos(\delta)\Big]^2\Big\}^{\frac{1}{2}}$$

$$l_8 = \Big\{\Big[b\sqrt{3}/3 - q_5 + A_2 + \big(b\sqrt{3}/6\big)\cos(q_1)\cos(q_2) + l\sin(\delta) \times \cos(\alpha + 30)\Big]^2 + \Big[A_1 - q_4 - \big(b\sqrt{3}/6\big)\sin(q_1)\cos(q_2) - l\sin(\delta)\sin(\alpha + 30)\Big]^2 + \Big[q_6 + (b/2)\cos(q_2)\sin(q_3) - \big(b\sqrt{3}/6\big)\sin(q_2) - l\cos(\delta)\Big]^2\Big\}^{\frac{1}{2}}$$

$$l_9 = \Big\{\Big[b/2 - q_4 + \big(b\sqrt{3}/3\big)\sin(q_1)\cos(q_2) + l\sin(\delta)\cos(\alpha)\Big]^2 + \Big[b\sqrt{3}/6 + q_5 + \big(b\sqrt{3}/3\big)\cos(q_1)\cos(q_2) - l\sin(\delta)\sin(\alpha)\Big]^2 + \Big[q_6 + \big(b\sqrt{3}/3\big)\sin(q_2) - l\cos(\delta)\Big]^2\Big\}^{\frac{1}{2}}$$

$$l_{10} = \Big\{\Big[b/2 - l\sin(\delta)\cos(\alpha) + q_4 - A_1 + \big(b\sqrt{3}/6\big)\sin(q_1)\cos(q_2)\Big]^2 + [A_3 - l\sin(\delta)\sin(\alpha) + q_5 - A_2]^2 + \Big[q_6 + (b/2)\cos(q_2)\sin(q_3) - \big(b\sqrt{3}/6\big)\sin(q_2) - l\cos(\delta)\Big]^2\Big\}^{\frac{1}{2}}$$

$$l_{11} = \Big\{\Big[l\sin(\delta)\cos(\alpha + 60) + q_4 - \big(b\sqrt{3}/3\big)\sin(q_1)\cos(q_2)\Big]^2 + [-l\sin(\delta)\sin(\alpha + 60) - q_5 + 2A_3]^2 + \Big[q_6 + \big(b\sqrt{3}/3\big)\sin(q_2) - l\cos(\delta)\Big]^2\Big\}^{\frac{1}{2}}$$

$$l_{12} = \Big\{\Big[b/2 - l\sin(\delta)\sin(\alpha + 30) - q_4 - A_1 - \big(b\sqrt{3}/6\big)\sin(q_1)\cos(q_2)\Big]^2 + [-A_3 + l\sin(\delta)\cos(\alpha + 30) - q_5 - A_2]^2 + \Big[-q_6 + (b/2)\cos(q_2)\sin(q_3) + \big(b\sqrt{3}/6\big)\sin(q_2) + l\cos(\delta)\Big]^2\Big\}^{\frac{1}{2}}$$

where the tendons are labeled as follows: tendon $1 = A_{12}B_{21}$, tendon $2 = A_{12}B_{11}$, tendon $3 = A_{22}B_{21}$, tendon $4 = A_{22}B_{31}$, tendon $5 = A_{32}B_{11}$, tendon $6 = A_{32}B_{31}$, tendon $7 = A_{11}A_{32}$, tendon $8 = A_{21}A_{12}$, tendon $9 = A_{31}A_{22}$, tendon $10 = B_{11}B_{12}$, tendon $11 = B_{21}B_{22}$, tendon $12 = B_{31}B_{32}$, and A_1, A_2, A_3 are given by

$$A_1 = (b/2)[\cos(q_1)\cos(q_3) - \sin(q_1)\sin(q_2)\sin(q_3)]$$

$$A_2 = (b/2)[\sin(q_1)\cos(q_3) + \cos(q_1)\sin(q_2)\sin(q_3)]$$

$$A_3 = \big(b\sqrt{3}/6\big)[1 - \cos(q_1)\cos(q_2)]$$

Appendix B: Matrix A_g

The elements of matrix A_g are given by

$$A_{g_{11}} = (b/D_1)\Big[b\cos(\psi_g + 30) + l\sqrt{3}\sin(\delta)\cos(\psi_g - \alpha)\Big]$$

$$A_{g_{12}} = (b/D_2)\Big[b\sin(\psi_g) + l\sqrt{3}\sin(\delta)\sin(\alpha - \psi_g - 30)\Big]$$

$$A_{g_{13}} = (b/S_1)\Big[b\cos(\psi_g + 30) + l\sqrt{3}\sin(\delta)\cos(\psi_g - \alpha - 60)\Big]$$

$$A_{g_{14}} = (b/S_2)\Big[b\sin(\psi_g) + l\sqrt{3}\sin(\delta)\cos(\psi_g - \alpha + 60)\Big]$$

$$A_{g_{21}} = (3/D_1)[l\cos(\delta) - h], \qquad A_{g_{22}} = (3/D_2)[l\cos(\delta) - h]$$

$$A_{g_{23}} = -(3h/S_1), \qquad A_{g_{24}} = -(3h/S_2)$$

Appendix C: Aerodynamic Coefficients

The aerodynamic coefficients of the aircraft are given as follows (all angles in radians):

$$C_d = C_d^l + C_d^{\delta_e} + C_d^{\delta_f}, \qquad C_l = C_l^{\alpha_a} + C_l^{\delta_e} + C_l^{\delta_f}$$

$$C_M = C_M^{\alpha_a} + C_M^{\delta_f} + C_M^{\delta_e} + C_M^0$$

$$C_l^{\alpha_a} = 0.3492 + 6.2083\alpha_a - 4.0012\alpha_a^2 - 5.727\alpha_a^3$$

$$C_l^{\delta_e} = \delta_e\big(0.40165 + 0.9437\alpha_a - 4.756\alpha_a^2\big)$$

$$C_l^{\delta_f} = \delta_f\big(1.153 - 0.2016\alpha_a - 3.993\alpha_a^2\big)$$

$$C_d^l = 0.01\Big[4.2084 + C_l^{\alpha_a}\big(-5.049 + 8.8544C_l^{\alpha_a}\big)\Big]$$

$$C_d^{\delta_e} = \delta_e\big(-0.0573 + 0.4815\alpha_a + 0.627\alpha_a^2\big)$$

$$C_d^{\delta_f} = \delta_f\big(0.1514 + 0.3226\alpha_a + 0.6544\alpha_a^2\big)$$

$$C_M^0 = -0.07, \qquad C_M^{\alpha_a} = -2.13\alpha_a + 0.46\alpha_a^2 + 1.73\alpha_a^3$$

$$C_M^{\delta_e} = \delta_e\big(-3 + 0.71\alpha_a + 4.1\alpha_a^2\big)$$

$$C_M^{\delta_f} = \delta_f\big(-0.92\alpha_a + 6.74\alpha_a^2\big)$$

References

[1]Parish, L., *Space-Flight Simulation Technology*, Howard W. Sams, Indianapolis, IN, 1969.

[2]Medeuil, C. C., "Evolution des Simulateurs d'Avions Civils," *Onde Electrique*, Vol. 68, No. 6, 1988, pp. 35–41.

[3]Sullivan, B., and Soukup, P., "The NASA Advanced Concepts Flight Simulator: A Unique Transport Research Environment," AIAA Paper 96-3517, July 1996.

[4]Blake, M., "The NASA Advanced Concepts Flight Simulator: A Unique Transport Research Environment," AIAA Paper 96-3518, July 1996.

[5]Repperger, D. W., "Study of Supermaneuverable Flight Trajectories Through Motion Field Simulation of a Centrifuge Simulator," *Journal of Dynamic Systems, Measurement, and Control*, Vol. 114, No. 2, 1992, pp. 270–277.

[6]Pouliot, N. A., Nahon, M. A., and Gosselin, C. M., "Analysis and Comparison of the Motion Simulation Capabilities of Three Degree of Freedom Flight Simulators," AIAA Paper 96-3474, July 1996.

[7]Parrish, R. V., Dieudonne, J. E., Bowles, R. L., and Martin, D. J. J., "Coordinated Adaptive Washout for Motion Simulators," *Journal of Aircraft*, Vol. 12, No. 1, 1975, pp. 44–50.

[8]Ariel, D., and Sivan, R., "False Cue Reduction in Moving Flight Simulators," *IEEE Transactions on Systems, Man, and Cybernetics*, Vol. 14, No. 4, 1984, pp. 665–671.

[9]Sturgeon, W. R., "Controllers for Aircraft Motion Simulators," *Journal of Guidance and Control*, Vol. 4, No. 2, 1981, pp. 184–191.

[10]Sivan, R., Ish-Shalom, J., and Huang, J. K., "An Optimal Control Approach to the Design of Moving Flight Simulators," *IEEE Transactions on Systems, Man, and Cybernetics*, Vol. 12, No. 6, 1982, pp. 818–827.

[11]Reid, L. D., and Nahon, M. A., "Response of Airline Pilots to Variations in Flight Simulator Motion Algorithms," *Journal of Aircraft*, Vol. 25, No. 7, 1988, pp. 639–646.

[12]Nahon, M. A., and Reid, L. D., "Simulator Motion Drive Algorithms: A Designer's Perspective," *Journal of Guidance, Control, and Dynamics*, Vol. 13, No. 2, 1990, pp. 356–361.

[13]Nahon, M. A., Reid, L. D., and Kirdeikis, J., "Adaptive Simulator Motion Software with Supervisory Control," *Journal of Guidance, Control, and Dynamics*, Vol. 15, No. 2, 1992, pp. 376–383.

[14]Idan, M., and Sahar, D., "A Robust Controller for a Dynamic Six Degree of Freedom Flight Simulator," AIAA Paper 96-3476, July 1996.

[15]Motro, R., "Tensegrity Systems: The State of the Art," *International Journal of Space Structures*, Vol. 7, No. 2, 1992, pp. 75–83.

[16]Snelson, K., "Snelson on the Tensegrity Invention," *International Journal of Space Structures*, Vol. 11, Nos. 1 and 2, 1996, pp. 43–48.

[17]Fuller, B., *Synergetics, Explorations in the Geometry of Thinking*, Collier Macmillan, London, 1975.

[18]Pugh, A., *An Introduction to Tensegrity*, Univ. of California Press, Berkeley, 1976.

[19]Pellegrino, S., and Calladine, C. R., "Matrix Analysis of Statically and Kinematically Indetermined Frameworks," *International Journal of Solids and Structures*, Vol. 22, No. 4, 1986, pp. 409–428.

[20]Motro, R., Najari, S., and Jouanna, P., "Static and Dynamic Analysis of Tensegrity Systems," *Proceedings of the International Symposium on Shell and Spatial Structures: Computational Aspects*, Springer–Verlag, New York, 1986, pp. 270–279.

[21]Hanaor, A., "Prestressed Pin-Jointed Structures—Flexibility Analysis and Prestress Design," *International Journal of Solids and Structures*, Vol. 28, No. 6, 1988, pp. 757–769.

[22]Furuya, H., "Concept of Deployable Tensegrity Structures in Space Application," *International Journal of Space Structures*, Vol. 7, No. 2, 1992, pp. 143–151.

[23]Skelton, R. E., and Sultan, C., "Controllable Tensegrity, A New Class of Smart Structures," *Proceedings of the International Society for Optical Engineering 4th Symposium on Smart Structures and Materials*, Vol. 3039, SPIE, Belligham, WA, 1997, pp. 166–177.

[24]Sultan, C., and Skelton, R. E., "Integrated Design of Controllable Tensegrity Structures," *Proceedings of the ASME Congress and Exposition*, Vol. 54, American Society of Mechanical Engineers, New York, 1997, pp. 27–37.

[25]Hanaor, A., "Aspects of Design of Double Layer Tensegrity Domes," *International Journal of Space Structures*, Vol. 7, No. 2, 1992, pp. 101–113.

[26]Wang, B. B., and Liu, X. L., "Integral Tension Research in Double Layer Tensegrity Grids," *International Journal of Space Structures*, Vol. 11, No. 4, 1992, pp. 165–172.

[27]Sultan, C., and Skelton, R. E., "Force and Torque Smart Tensegrity Sensor," *Proceedings of the International Society for Optical Engineering 5th Symposium on Smart Structures and Materials*, Vol. 3323, SPIE, Belligham, WA, 1998, pp. 357–368.

[28]Sultan, C., Corless, M., and Skelton, R. E., "Peak to Peak Control of an Adaptive Tensegrity Space Telescope," *Proceedings of the International Society for Optical Engineering 5th Symposium on Smart Structures and Materials*, Vol. 3323, SPIE, Belligham, WA, 1999, pp. 190–201.

[29]Zenieh, S., and Corless, M., "Simple Robust $r - \gamma$ Tracking Controllers for Uncertain Fully Actuated Mechanical Systems," *Journal of Dynamic Systems, Measurement, and Control*, Vol. 119, No. 4, 1997, pp. 821–825.

[30]Spong, M. W., "On the Robust Control of Robot Manipulators," *IEEE Transactions on Automatic Control*, Vol. 37, No. 11, 1992, pp. 1782–1786.

[31]Corless, M., "Control of Uncertain Nonlinear Systems," *Journal of Dynamic Systems, Measurement, and Control*, Vol. 115, No. 2(B), 1993, pp. 471–484.

[32]Sultan, C., "Stability and Control of the Airplane at High Angles of Attack; Bifurcation Phenomena," *Revue Roumaine des Sciences Techniques—Mecanique Appliquee*, Vol. 39, No. 6, 1994, pp. 693–706.